

Light-field imaging from position-momentum correlations

Davide Giannella^{a,b}, Gianlorenzo Massaro^{a,b}, Bohumil Stoklasa^c,
Milena D'Angelo^{a,b,*}, Francesco V. Pepe^{a,b}

^a*Dipartimento Interuniversitario di Fisica, Università degli studi di Bari, I-70126 Bari, Italy*

^b*INFN, Sezione di Bari, I-70126 Bari, Italy*

^c*Department of Optics, Palacký University, 77146 Olomouc, Czech Republic*

Abstract

Correlation plenoptic imaging (CPI) is a light-field imaging technique employing intensity correlation measurements to simultaneously detect the spatial distribution and the propagation direction of light. Compared to standard methods, in which light-field images are directly encoded in intensity, CPI provides a significant enhancement of the volumetric reconstruction performance in terms of both achievable depth of field and 3D resolution. In this article, we present a novel CPI configuration where light-field information is encoded in correlations between position and momentum measurements, namely, points on a given object plane and points of the Fourier plane of the imaging lens. Besides the fundamental interest in retrieving the properties of position-momentum correlation, the proposed scheme overcomes practical limitations of previously proposed setups, providing higher axial homogeneity and robustness with respect to the identification of reference planes.

1. Introduction

In the rapidly-developing field of 3D imaging techniques, light-field (or *plenoptic*) imaging is one of the most promising and used. Light-field devices can measure simultaneously, without the need for moving parts, both the light distribution from the scene of interest and the propagation direction of

*milena.dangelo@uniba.it

light rays [1, 2, 3]. The availability of directional information makes single-shot volumetric reconstruction possible, whereas a standard imaging system would require multiple acquisitions on a series of independent axial planes to obtain a similar amount of information.

One of the main reasons behind the success of light-field imaging is the structural simplicity of the devices, essentially consisting of standard cameras integrated with an array of microlenses between the main lens and the sensor. Such a structure ensures contained costs and high acquisition speed, which makes light-field imaging popular in the most diverse fields, ranging from photography to microscopy [4, 5, 6], for cutting-edge application such as imaging of neuronal activity [7] and wavefront sensing [8]. Nonetheless, traditional light-field devices such as those described above suffer from a limitation in the best resolution that can be achieved, due to the fact that a *single* sensor captures a composite information, in which both the spatial distribution and the direction of light are encoded [9, 10].

An alternative method to light-field imaging capable of addressing the resolution loss has recently emerged in the context of correlation imaging [11, 12, 13, 14, 15, 16, 17]. In this approach, called correlation plenoptic imaging (CPI), the plenoptic information is split over two separate sensors, both endowed with spatial resolution [18, 19, 20]. While a simple intensity measurement on each detector does not contain volumetric information, the latter is encoded in the correlation between intensity fluctuations registered at each pair of pixels of the disjoint sensors. Besides recovering Rayleigh-limited resolution of focused images, CPI has further advantages deriving from an unparalleled extension of the longitudinal depth along which the sample can be correctly reconstructed starting from a single plenoptic image [21, 22, 23]. Since its introduction, great improvement to the performance of the device have been carried over, both in terms of its optical performance [22, 23] and signal-to-noise ratio optimization [24, 25], to obtain remarkable performance in microscopy applications [26] and in acquisition speed [27].

In this article, we present a novel CPI configuration, based on measuring correlations between position and momentum measurements: the first one being measured in points on a given object plane, close to the imaged sample, and the second one in points of the Fourier plane of the imaging lens [28]. Previous CPI setups were based on the fact that intensity correlations encode images of the same scene, as if it were illuminated by different point sources. Compared to microlens-based light-field techniques (even using correlation measurements in so-called ghost imaging, see Ref. [29]), CPI

potentially provides a much wider variety of independent viewpoints on a 3D sample. However, such an interesting property has practical drawbacks, such as the sensitivity to the axial distances of planes that are difficult to identify and the dependence of image magnification on the axial position (see Ref. [21]). Here, we will show how using position-momentum correlation measurement, besides its fundamental interest, also helps to overcome even such technical problems of CPI.

The article is organized as follows. In Section 2, we illustrate the plenoptic capability of the proposed correlation measurement protocol, offering a theoretical demonstration of its working principle. In Section 3, we characterize the refocusing capability of the protocol by using Gaussian test objects and a numerical simulation applied to a planar target. The capability of the proposed CPI scheme to overcome the mentioned drawbacks of previous CPI protocols is discussed in Section 4, together with a summary of the main results.

2. Plenoptic properties of intensity correlations

A simple setup for measuring correlations between the near-field and the far-field of a sample is schematically represented in Fig. 1. Light emitted from an object S propagates through a two-lens system made of a first converging lens L_1 with focal length f_1 and a second converging lens L_2 with focal length f_2 and is collected by a detector D_A placed in the second focal plane of the second lens. This detector, endowed with spatial resolution, collects the image of the intensity distribution on the first focal plane of L_1 , reversed and magnified by a factor $M = f_2/f_1$. A second detector D_B is placed directly in the second focal plane of L_1 (i.e., in the Fourier plane), giving access to far-field information; light is then deflected towards D_B by means of a beam splitter (BS) placed between the two lenses, so that part of the intensity coming from the first lens in D_B is moved in an orthogonal path. Let us call $I_A(\boldsymbol{\rho}_A)$ and $I_B(\boldsymbol{\rho}_B)$ the intensity distributions collected by D_A and D_B , respectively, where $\boldsymbol{\rho}_A$ and $\boldsymbol{\rho}_B$ are two-dimensional transverse spatial coordinates defined on the photo-sensitive planes of the two detectors. It is worth noticing that the main lens Fourier plane, in cases when it is physically inaccessible such as in most microscope objectives, can be imaged on a farther plane by using a relay imaging system.

By correlating, pixel by pixel, the signal at the two detectors, a *position-momentum* correlation is measured. If the object emits (or transmits or

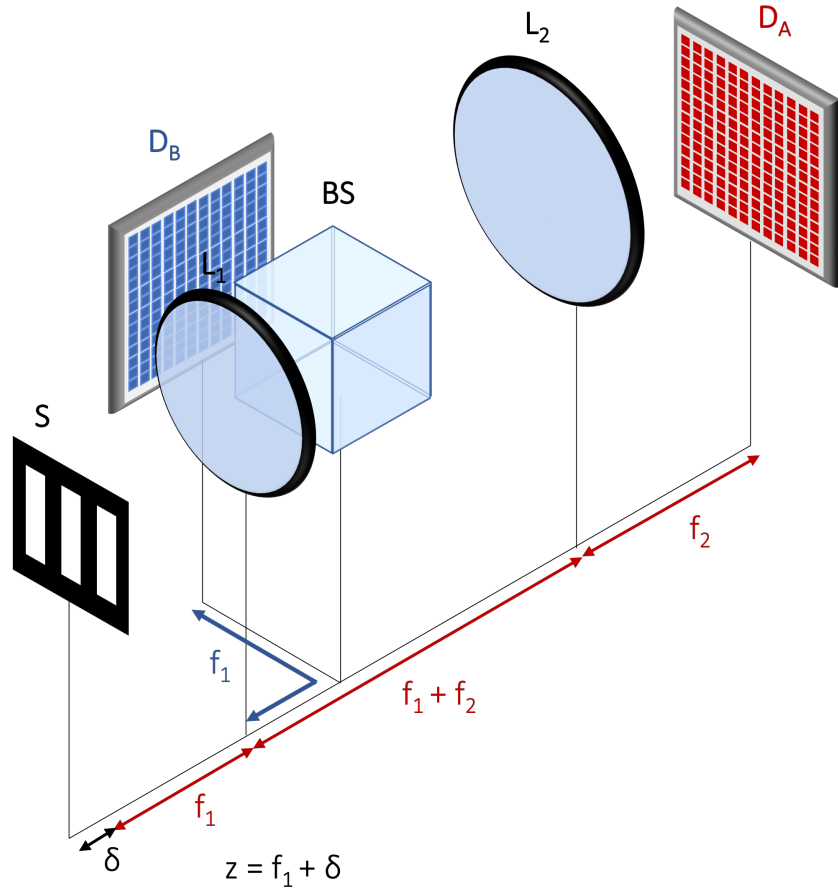


Figure 1: A schematic representation of the setup: the object, represented as a flat triple slit S and treated as a chaotic light emitter, is placed at a distance $z = f_1 + \delta$ from the first lens L_1 of a two-lenses system, in a f - f configuration, composed of L_1 with focal length f_1 and L_2 with focal length f_2 ; the two lenses are separated by a distance $f_1 + f_2$. The detector D_A is in the second focal plane of the second lens, which is, in the conjugate plane of the first focal plane of L_1 . In the space between the two lenses, a beam splitter BS deviates half of the intensity in the second arm of the setup toward the detector D_B , which is placed in the Fourier plane of the first lens.

reflects) thermal light [30], this correlation contains plenoptic information [18]. In general, the relevant information is contained in the second order correlation function $\Gamma^{(2)}$, the four dimensional function representing the correlations between the intensity fluctuations defined as

$$\Gamma^{(2)}(\boldsymbol{\rho}_A, \boldsymbol{\rho}_B) = \langle I_A(\boldsymbol{\rho}_A) I_B(\boldsymbol{\rho}_B) \rangle - \langle I_A(\boldsymbol{\rho}_A) \rangle \langle I_B(\boldsymbol{\rho}_B) \rangle \quad (1)$$

where the $\langle \dots \rangle$ denotes the ensemble average over the different statistical realizations of the intensity distributions. To better visualize the plenoptic capabilities contained in $\Gamma^{(2)}$ and how these can lead to refocusing out-of-focus objects, we consider a two-dimensional object with emission profile $\mathcal{A}(\boldsymbol{\rho}_s)$, shining quasi-monochromatic thermal light on the optical apparatus, placed at a distance z from the first lens L_1 . By using the paraxial optics transfer functions to propagate the fields [28], and assuming negligible coherence area [31] at the object plane (i.e., the object is considered as a source of incoherent light), the second order correlation function can be calculated and reads, up to irrelevant constant factors:

$$\Gamma^{(2)}(\boldsymbol{\rho}_a, \boldsymbol{\rho}_b) \sim \left| \int_{-\infty}^{+\infty} d^2 \boldsymbol{\rho}_s |\mathcal{A}(\boldsymbol{\rho}_s)|^2 \int_{-\infty}^{+\infty} d^2 \boldsymbol{\rho}_1 \mathcal{P}_{L_1}(\boldsymbol{\rho}_1) \times \int_{-\infty}^{+\infty} d^2 \boldsymbol{\rho}'_1 \mathcal{P}_{L_1}(\boldsymbol{\rho}'_1) e^{i\phi(\boldsymbol{\rho}_s, \boldsymbol{\rho}_1, \boldsymbol{\rho}'_1, \boldsymbol{\rho}_A, \boldsymbol{\rho}_B)} \right|^2 \quad (2)$$

where we have considered the aperture of the lens L_1 , as described by the pupil function $\mathcal{P}_{L_1}(\boldsymbol{\rho}_1)$ (namely, a real function representing the geometrical shape of the lens), to be the relevant aperture of the system, thus neglecting the one of the second lens, treated as infinite. The term ϕ calculated in the coordinates of the sample, the first lens and the detectors, is characteristic of the specific protocol and reads

$$\phi(\boldsymbol{\rho}_s, \boldsymbol{\rho}_1, \boldsymbol{\rho}'_1, \boldsymbol{\rho}_A, \boldsymbol{\rho}_B) = k \left[\left(\frac{1}{z} - \frac{1}{f_1} \right) \frac{\boldsymbol{\rho}_1^2}{2} - \boldsymbol{\rho}_1 \cdot \left(\frac{\boldsymbol{\rho}_s}{z} + \frac{\boldsymbol{\rho}_A}{f_2} \right) - \frac{\boldsymbol{\rho}'_1{}^2}{2z} + \boldsymbol{\rho}'_1 \cdot \left(\frac{\boldsymbol{\rho}_s}{z} + \frac{\boldsymbol{\rho}_B}{f_1} \right) \right] \quad (3)$$

where $k = \frac{2\pi}{\lambda}$ is the wavenumber and λ the central wavelength of the quasi-monochromatic emission. The integral in Eq. (2) can be solved in the geometrical optics limit using a stationary phase approximation [32]. Calling $\boldsymbol{\rho}_j = (x_j, y_j)$, with $j = A, B$, we can further simplify the result writing the $\Gamma^{(2)}$ as a two-variable function factorized in a geometrical part $\Gamma_{geom}^{(2)}(x_A, x_B)$

involving the object-related information leading to refocusing and a factor involving apertures $\Gamma_{pupils}^{(2)}(x_A, x_B) = |\mathcal{P}_{L_1}(x_A, x_B)|^4$ [33]. The first term can be written as

$$\Gamma_{geom}^{(2)}(x_A, x_B) = \left| \mathcal{A} \left(-\frac{x_A}{M} + \left(1 - \frac{z}{f_1} \right) x_B \right) \right|^4. \quad (4)$$

The geometrical meaning of the correspondence between an object point x_s and the two detector coordinates, as contained in this function, becomes evident by inserting a real parameter $z = f_1 + \delta$, with δ the defocusing parameter, defining the out-of-focus distance at which the object is placed; with this substitution, Eq. (4) becomes

$$\Gamma_{geom}^{(2)}(x_A, x_B) = \left| \mathcal{A} \left(-\frac{x_A}{M} - \delta \frac{x_B}{f_1} \right) \right|^4.$$

In this expression, we can recognize the quantity x_B/f_1 , given by the ratio between the position of a point in the Fourier plane and the focal length of the first lens L_1 , as representing the angle of propagation from the object plane to the lens. By fixing this coordinate, all rays propagating at this angle from all the object points can be reconstructed. Concurrently, the term $-x_A/M$ represents a point in the first focal plane of L_1 . Fixing the coordinates x_B and x_A uniquely selects, among the rays propagating at the angle x_B/f_1 , the one passing through $-x_A/M$. The knowledge of the parameter δ completes the identification of a single point x_s on the object. Formally, this correspondence represents a line $(\gamma_s(x_s) : -\frac{x_A}{M} - \frac{\delta}{f_1} x_B = x_s)$ in the (x_A, x_B) space, along which it is convenient to integrate the $\Gamma^{(2)}(x_A, x_B)$ to reconstruct the refocused image [34, 33]. In the geometrical approximation in which we are working, this general integration can be written

$$\begin{aligned} \Sigma(x_s) &= \int_{\gamma_s(x_s)} \Gamma^{(2)}(x_A, x_B) d\ell = \int_{\gamma_s(x_s)} \Gamma_{geom}^{(2)}(x_A, x_B) \Gamma_{pupils}^{(2)}(x_A, x_B) d\ell \\ &= \int_{\gamma_s(x_s)} \left| \mathcal{A} \left(-\frac{x_A}{M} - \frac{\delta}{f_1} x_B \right) \right|^4 |\mathcal{P}_{L_1}(x_A, x_B)|^4 d\ell \sim |\mathcal{A}(x_s)|^4, \end{aligned} \quad (5)$$

considering that the artifacts to the object reconstruction created by the presence of the $\Gamma_{pupils}^{(2)}(x_A, x_B)$ term can easily be corrected [33].

It is worth noticing that the magnification of all the object sub-images, obtained for each x_B and concurring to the formation of the refocused image,

is independent of the object axial position and coincides with the native magnification M of focused images. Such a feature, unique in the context of CPI, ensures an increased homogeneity of the image properties of axially extended samples.

3. Imaging performance of CPI based on position-momentum measurements

The adoption of the geometrical approximation is convenient to explicitly retrieve both the correspondence between detector and object coordinates encoded in $\Gamma^{(2)}$ and the lines along which to integrate to obtain refocusing. However, this approach does not give evidence of the wave-optics effects of propagation and diffraction resulting in the definition of resolution and depth of field. To quantitatively show how CPI refocusing translates into an enhancement of the depth of field with respect to standard imaging, we consider a Gaussian object with intensity profile $|\mathcal{A}(x_s)|^2 = \exp\left(-\frac{x_s^2}{2\sigma_s^2}\right)$ and standard deviation σ_s defined by its linear size, and place it at a distance δ from the first focal plane of L_1 ; we then calculate both its refocused image for the specific δ (as given by the proposed CPI protocol, but without the application of the stationary phase approximations) and its standard image, as acquired directly by the detector D_A . The spreading in transverse dimension of both these images is finally evaluated for varying δ and σ_s .

To obtain the refocused image analytically, we assume a Gaussian approximation for the pupil function ($|\mathcal{P}_{L_1}(x_1)|^2 = \exp\left(-\frac{x_1^2}{2\sigma_1^2}\right)$) and calculate $\Gamma^{(2)}$ by means of Eq. (2); we then apply the refocusing integration of Eq. (5) and obtain again a Gaussian function with standard deviation $\sigma_{CPI}(\sigma_s, \delta)$ dependent on both the size and the position of the object. Using the paraxial propagators of the electric field, we calculate the standard image acquired by the detector D_A and we call $\sigma_{SI}(\sigma_s, \delta)$ its transverse dimension also dependent on σ_s and δ . To perform a comparison, we conventionally consider, for each defocusing δ and width σ_s , the regions in which $\sigma_{CPI}(\sigma_s, \delta)$ and $\sigma_{SI}(\sigma_s, \delta)$ are smaller than $1.2 \sigma_s$ (*i.e.* the image spread is smaller than 20% of the original object size). The results are presented in Fig. 2, where the vertical and horizontal axes report, respectively, the transverse dimensions of the object σ_s and the defocusing parameter δ at which the object is placed: the green and red solid contour lines represent the threshold on which the transverse dimension of the image is broadened by 20% due to loss of resolution (namely, when the image size becomes 1.2 times the dimension of

the object), for CPI and standard imaging respectively; the green and red tilted lines fill the regions in which the dimension of the images is below this threshold.

This plot can be interpreted as an indication of the different behavior of resolution as the object is moved from the focal plane, in the two imaging techniques. Similar trends can be observed in the visibility-based resolution limits described in Refs. [20, 22]. Notice, however, that curves in Fig. 2 do not directly carry information about the visibility of the image of two separated object points: σ_s can be viewed as the detail size on the object side and the colored regions indicate, for each distance from the focal plane, the detail size that can be imaged by the two protocols with a spreading below a certain threshold, which is set to 20% as an arbitrary reference. The trends in Fig. 2 provide a qualitative indication of the loss of resolution with distance from the focal plane.

The comparison between the two protocols, in particular, shows how, outside of the natural depth of field of the system, while for standard imaging the degradation of resolution scales approximately linearly with the distance from the focal plane, exploiting correlations between position and momentum allows this trend to become a square root of the same distance, leading to a slower loss of details, typical of CPI protocols [20, 22, 23].

It is finally worth pointing out the difference in behavior of the two protocols in the focal plane of L_1 for $\delta = 0$: the lower spreading (hence, better resolution) associated to CPI is due to the second order correlation measurement in the process of image formation and should not be interpreted as a characteristic of the optical system. The correlation-based imaging process, as can be clearly understood by the third integral of Eq. (5), involves the integration over the second power of the intensity of the object whose size, for a Gaussian object, is $1/\sqrt{2}$ the size of the object itself. This means that, for Gaussian objects, the variance of the produced image is the sum of the squares of a diffractive term, which depends on the numerical aperture of the system and on the wavelength λ , and the original object size divided by a factor $\sqrt{2}$; for standard imaging, the diffractive term is the same, but the second term in the sum is the object size σ_s itself.

To show an example of the refocusing properties of the position-momentum based CPI protocol, we simulate the measurement of a correlation function in the experimental situation discussed above and apply the refocusing procedure reported in Eq. (5) to obtain refocusing. In particular, we consider a two-dimensional object placed at a distance $\delta = +1$ mm away from the

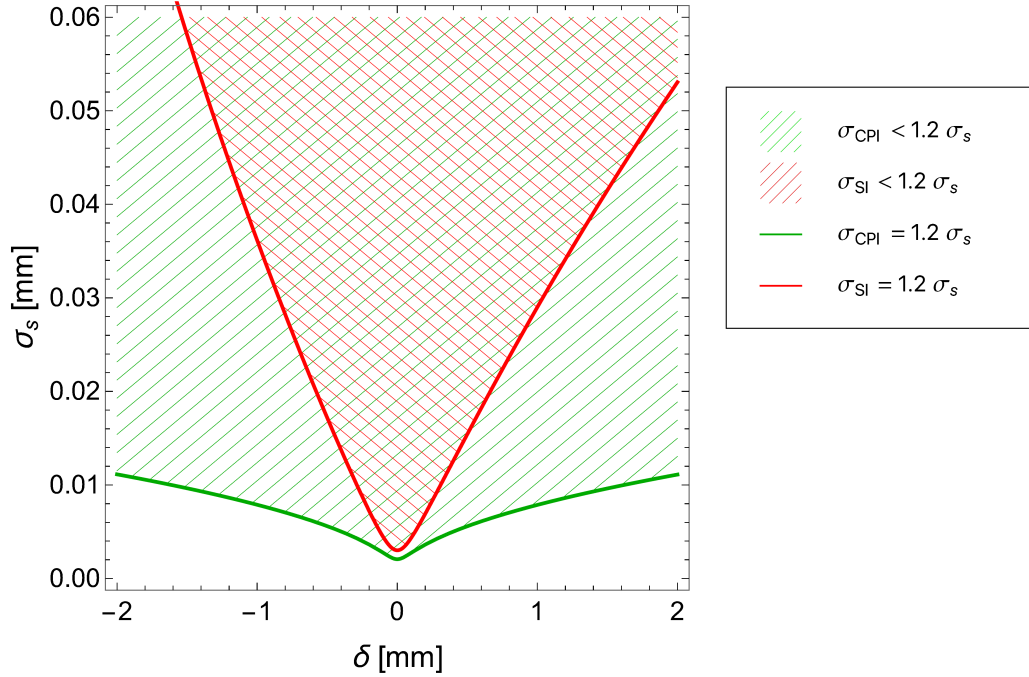


Figure 2: An analytical resolution against depth of field comparison between the CPI protocol discussed in the text and standard imaging, performed calculating how should vary the size of a Gaussian intensity object of width σ_s and its distance from the focal plane δ , to be imaged with a width below a certain threshold. In particular, the region filled with tilted green lines indicates the values of σ_s and the positions δ producing refocused images with a linear size σ_{CPI} that is less than 20% of the original object size while the region filled with red tilted lines the values of σ_s and δ producing standard images of size σ_{SI} less than the 20% of the object width. The green and red solid lines represent the boundaries of these regions on which the image size is exactly 1.2 times σ_s , for CPI and standard imaging, respectively. The presented curves are calculated for $M = 1$, $f_1 = f_2 = 30$ mm, $\sigma_1 = 0.635$ mm, $\lambda = 532$ nm and sample characterized by full transversely incoherent emission.

first focal plane of the first lens L_1 (plane at focus). The object is a mask composed by three perfectly transmissive rectangular slits, having center-to-center distance of $50 \mu\text{m}$.

The incoherent emission from the target is simulated by computing a series of speckle patterns [35] following pseudo-random thermal statistics and propagating them along the two arms of the setup to reach the two detectors (with no modifications to the statistics of the incoming light due to the presence of the beam splitter), and then obtaining the two intensity distributions $I_A(\boldsymbol{\rho}_A)$ and $I_B(\boldsymbol{\rho}_B)$ by collecting N statistically independent frames. By using Eq. (1) and an ergodic hypothesis, we are now able to calculate the correlation function; the simulated second order correlation function shall be indicated as $\Gamma_{sim}^{(2)}$.

In the left panel of Fig. 3, we report the calculated standard image as acquired by the detector D_A : the triple slit appears completely blurred since the mask is placed far beyond the natural depth of field of the two-lens system. The image is obtained by simply averaging all the $I_A(\boldsymbol{\rho}_A)$ distributions acquired over the N frames. In the right panel, we report the perfectly resolved refocusing of the object performed by taking advantage of the plenoptic content of the correlation function, as obtained by applying directly the first integral of Eq. (5) to $\Gamma_{sim}^{(2)}$. In the numerical simulation, the magnification of the two-lens system is set to $M = 1$, the lens L_1 acts as a thin lens with numerical aperture $\text{NA} = 0.05$ and focal length $f_1 = 30 \text{ mm}$ and the chosen number of frames is $N = 15000$.

4. Summary and discussion

We have presented a novel protocol to perform correlation plenoptic imaging based on the measurement of correlations between intensity fluctuations occurring in the object plane and in the Fourier plane of a two-lens system, *i.e.* exploiting position-momentum correlations. Starting with a geometrical approximation, we have demonstrated the plenoptic capability of the protocol and derived the so-called *refocusing algorithm*, namely, the coordinate transformation to be applied to the measured correlation function $\Gamma^{(2)}$; such transformation is just the path over which performing the linear integration of $\Gamma^{(2)}$ to recover the image of the out-of-focus object. The trend of the resolution as a function of the depth of field of the proposed CPI protocol has highlighted the square-root scaling responsible for the wide depth of field enhancement of CPI (compared to the linear scaling of standard imaging).

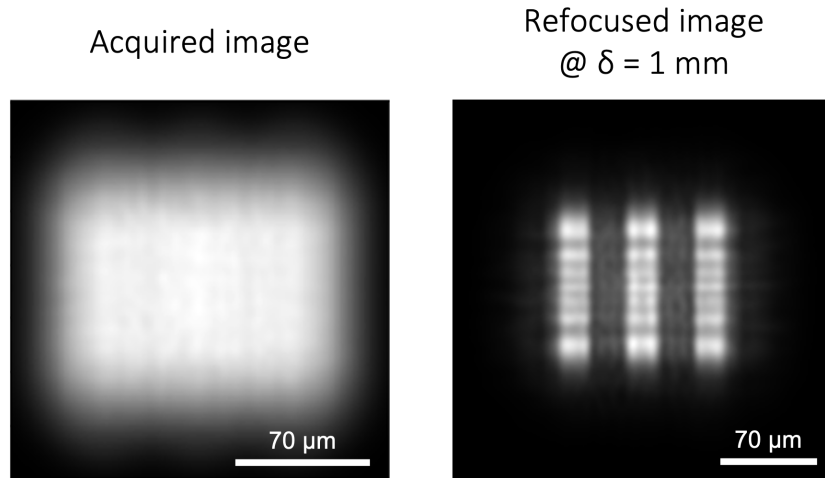


Figure 3: Left: simulation of the intensity acquired by the detector D_A over the collected N frames, representing the completely blurred image of the mask placed at $\delta = 1$ mm from the L_1 lens first focal plane, outside the depth of field of the two-lenses system. Right: refocused image of the same mask placed in the same position, reconstructed by exploiting the plenoptic information contained in $\Gamma_{sim}^{(2)}$, the correlation function calculated from the simulated frames collected by the two detectors D_A and D_B , as retrieved after the application of the first integral of Eq. (5). The scale bar indicates approximately $70 \mu\text{m}$. Notice that the parameters of the main lens used in the simulation are matched with those of the Gaussian lens used for Fig. 2, by requiring that the two lenses yield the same visibility when imaging two separated point sources on the focus plane.

The presented numerical simulation has also shown the result obtained by refocusing the image of $50\ \mu\text{m}$ slit, placed 1 mm out of focus, outside the region of resolvable details for standard imaging. This completes the demonstration of the functionality of the proposed correlation plenoptic imaging scheme, confirming the flexibility of CPI protocols in the choice of planes over which measuring correlations.

An outstanding feature of the proposed protocol is the fact that the sub-images obtained by selecting different illumination direction are characterized by the same magnification, regardless of the axial distance from the main lens. Such a feature, bearing an interesting parallelism with telecentric imaging systems, ensures a much larger homogeneity of the refocused images along the axial direction, which was not incorporated in the previous CPI schemes, where *points* of illumination, instead of *directions*, can be naturally selected from correlations of intensity fluctuations.

Moreover, it is worth noticing that the optical performance of the proposed implementation is similar to the one characterizing the microscopy-oriented CPI setup discussed in Ref. [26]), where correlations are measured between the near-field of the object, imaged through a conventional microscope, and the light intensity on the first lens surface. Although theoretically well-defined in the thin-lens approximation, the latter configuration is not as simple to reproduce experimentally when thick lenses are involved. In these cases, the imaged plane is either chosen between the lens principal planes, or any other plane within the optical component. However, these planes are typically not easily accessible experimentally, do not always show distinctive optical features, and can only be determined with a certain degree of uncertainty. For these reasons, the refocusing procedure needs accurate calibration in order to determine the appropriate coefficients. Imaging the Fourier plane as we propose here, instead, removes all the uncertainties in this regard, since the second focal plane is always well-defined even for real optical components and is easily recognized experimentally due to its distinctive optical features.

Author contributions

Conceptualization: all authors; methodology: D.G., G.M., M.D., F.V.P.; software: G.M.; formal analysis: D.G., G.M.; validation: B.S., M.D., F.V.P.; writing–original draft preparation: D.G., G.M.; writing–review and editing: all authors; visualization: D.G., G.M.; supervision: F.V.P., M.D.; project

administration: M.D.; funding acquisition: M.D., B.S. All authors have read and agreed to the submitted version of the manuscript.

Acknowledgments

The research is supported by project Qu3D, funded by the Italian Istituto Nazionale di Fisica Nucleare, the Swiss National Science Foundation (grant 20QT21 187716 “Quantum 3D Imaging at high speed and high resolution”), the Greek General Secretariat for Research and Technology, the Czech Ministry of Education, Youth and Sports, under the QuantERA programme, which has received funding from the European Union’s Horizon 2020 research and innovation programme. D.G., G.M., M.D. and F.V.P. are supported by Istituto Nazionale di Fisica Nucleare (INFN) through project QUISS. M.D. is supported by European Union-NextGenerationEU PE0000023 - “National Quantum Science and Technology Institute”. F.V.P. is supported by European Union-NextGenerationEU CN00000013 - “National Centre for HPC, Big Data and Quantum Computing”.

References

- [1] E. H. Adelson, J. Y. A. Wang, Single lens stereo with a plenoptic camera, *IEEE Trans. Pattern Anal. Mach. Intell.* 14 (1992) 99–106.
- [2] G. Wu, B. Masia, A. Jarabo, Y. Zhang, L. Wang, Q. Dai, T. Chai, Y. Liu, Light Field Image Processing: An Overview, *IEEE J. Sel. Top. Signal Process.* 11 (2017) 926–954.
- [3] E. Y. Lam, Computational photography with plenoptic camera and light field capture: tutorial, *J. Opt. Soc. Am. A* 32 (2015) 2021–2032.
- [4] R. NG, M. Levoy, M. Brédif, G. Duval, M. Horowitz, Pat Hanrahan, Light field photography with a hand-held plenoptic camera, Stanford University Computer Science Tech Report CSTR 2005-02 (April 2005).
- [5] R. Ng, Fourier Slice Photography, *ACM Trans. Graph.* 24 (2005) 735–744.
- [6] M. Broxton, L. Grosenick, S. Yang, N. Cohen, A. Andalman, K. Deiseroth, M. Levoy, Wave optics theory and 3-d deconvolution for the light field microscope, *Opt. Express* 21 (2013) 25418–25439.

- [7] R. Prevedel, Y.-G. Yoon, M. Hoffmann, N. Pak, G. Wetzstein, S. Kato, T. Schrödel, R. Raskar, M. Zimmer, E. S. Boyden, A. Vaziri, Simultaneous whole-animal 3d imaging of neuronal activity using light-field microscopy, *Nat. Methods* 11 (2014) 727–730.
- [8] J. Ko, C. C. Davis, Comparison of the plenoptic sensor and the shack-hartmann sensor, *Appl. Opt.* 56 (2017) 3689–3698.
- [9] T. Georgeiv, K. C. Zheng, B. Curless, D. Salesin, S. K. Nayar, C. Intwala, Spatio-angular resolution tradeoffs in integral photography, in: *EGSR '06: Proceedings of the 17th Eurographics conference on Rendering Techniques*, 2006, pp. 263–272.
- [10] B. Goldluecke, O. Klehm, S. Wanner, E. Eisemann, *Plenoptic Cameras*, CRC Press, 2015, Ch. Digital Representations of the Real World: How to Capture, Model, and Render Visual Reality, pp. 65–77.
- [11] T. B. Pittman, Y.-H. Shih, D. V. Strekalov, A. V. Sergienko, Optical imaging by means of two-photon quantum entanglement, *Phys. Rev. A* 52 (1995) R3429.
- [12] R. S. Bennink, S. J. Bentley, R. W. Boyd, “Two-photon” coincidence imaging with a classical source, *Phys. Rev. Lett.* 89 (2002) 113601.
- [13] A. Valencia, G. Scarcelli, M. D’Angelo, Y. Shih, Two-photon imaging with thermal light, *Phys. Rev. Lett.* 94 (2005) 063601.
- [14] A. Gatti, E. Brambilla, M. Bache, L. A. Lugiato, Ghost imaging with thermal light: comparing entanglement and classical correlation, *Phys. Rev. Lett.* 93 (2004) 093602.
- [15] G. Scarcelli, V. Berardi, Y. Shih, Can two-photon correlation of chaotic light be considered as correlation of intensity fluctuations?, *Phys. Rev. Lett.* 96 (2006) 063602.
- [16] M. N. O’Sullivan, K. W. C. Chan, R. W. Boyd, Comparison of the signal-to-noise characteristics of quantum versus thermal ghost imaging, *Phys. Rev. A* 82 (2010) 053803.
- [17] G. Brida, M. Chekhova, G. Fornaro, M. Genovese, E. Lopaeva, I. R. Berchera, Systematic analysis of signal-to-noise ratio in bipartite ghost

- imaging with classical and quantum light, *Phys. Rev. A* 83 (2011) 063807.
- [18] M. D'Angelo, F. V. Pepe, A. Garuccio, G. Scarcelli, Correlation plenoptic imaging, *Phys. Rev. Lett.* 116 (2016) 223602.
 - [19] F. Pepe, F. Di Lena, A. Garuccio, G. Scarcelli, M. D'Angelo, Correlation Plenoptic Imaging With Entangled Photons, *Technologies* 4 (2016).
 - [20] F. V. Pepe, F. Di Lena, A. Mazzilli, E. Edrei, A. Garuccio, G. Scarcelli, M. D'Angelo, Diffraction-limited plenoptic imaging with correlated light, *Phys. Rev. Lett.* 119 (2017) 243602.
 - [21] F. Di Lena, F. Pepe, A. Garuccio, M. D'Angelo, Correlation Plenoptic Imaging: An Overview, *Appl. Sci.* 8 (2018) 1958.
 - [22] A. Scagliola, F. Di Lena, A. Garuccio, M. D'Angelo, F. V. Pepe, Correlation plenoptic imaging for microscopy applications, *Phys. Lett. A* 384 (2020) 126472.
 - [23] F. D. Lena, G. Massaro, A. Lupo, A. Garuccio, F. V. Pepe, M. D'Angelo, Correlation plenoptic imaging between arbitrary planes, *Opt. Express* 28 (2020) 35857–35868.
 - [24] G. Scala, M. D'Angelo, A. Garuccio, S. Pascazio, F. Pepe, Signal-to-noise properties of correlation plenoptic imaging with chaotic light, *Phys. Rev. A* 99 (2019) 053808.
 - [25] G. Massaro, G. Scala, M. D'Angelo, F. V. Pepe, Comparative analysis of signal-to-noise ratio in correlation plenoptic imaging architectures, *Eur. Phys. J. Plus* 137 (2022) 1123.
 - [26] G. Massaro, D. Giannella, A. Scagliola, F. Di Lena, G. Scarcelli, A. Garuccio, F. V. Pepe, M. D'Angelo, Light-field microscopy with correlated beams for high-resolution volumetric imaging, *Sci. Rep.* 12 (2022) 16823.
 - [27] G. Massaro, P. Mos, S. Vasiukov, F. D. Lena, F. Scattarella, F. V. Pepe, A. Ulku, D. Giannella, E. Charbon, C. Bruschini, M. D'Angelo, Correlated-photon imaging at 10 volumetric images per second, *Sci. Rep.* 13 (2023) 12813.

- [28] J. W. Goodman, Introduction to Fourier optics, 3rd ed., Macmillan Learning, London, 2005.
- [29] A. Paniate, G. Massaro, A. Avella, A. Meda, F. V. Pepe, M. Genovese, M. D'Angelo, I. Ruo Berchera, Light Field Ghost Imaging, arXiv preprint arXiv:2309.14701 (2023).
- [30] L. Mandel, E. Wolf, Optical Coherence and Quantum Optics, Cambridge University Press, Cambridge, 1995.
- [31] B. Saleh, M. Teich, Fundamentals of Photonics, John Wiley & Sons, Hoboken, NJ, 2013.
- [32] R. Wong, Asymptotic Approximations of Integrals, Society for Industrial and Applied Mathematics, 2001.
- [33] G. Massaro, F. Di Lena, M. D'Angelo, F. V. Pepe, Effect of finite-sized optical components and pixels on light-field imaging through correlated light, Sensors 22 (2022) 2778.
- [34] G. Massaro, F. V. Pepe, M. D'Angelo, Refocusing algorithm for correlation plenoptic imaging, Sensors 22 (2022) 6665.
- [35] J. W. Goodman, Speckle Phenomena in Optics: Theory and Applications, 2nd ed., SPIE Press, Bellingham, WA, 2007.